Energy Materials

Supplementary Materials

Superhydrophobicity-enabled triphase interfacial microenvironment for high-temperature CO_2-to-formate electrocatalysis

Weiyan Wang[1,#], Kaixin Li[1,#], Siyu Zou[2,#], Lihui Huang[1], Xia Sheng[1], Jun Zhang[1,*], Xinjian Feng[1,*]

[1]State Key Laboratory of Bioinspired Interfacial Materials Science, College of Chemistry, Chemical Engineering and Materials Science, Soochow University, Suzhou 215123, Jiangsu, China.

[2]College of Chemical Engineering, Xiangtan University, Xiangtan 411105, Hunan, China.

[#]These authors contributed equally to this work.

***Correspondence to:** Prof. Xinjian Feng, Dr. Jun Zhang, State Key Laboratory of Bioinspired Interfacial Materials Science, College of Chemistry, Chemical Engineering and Materials Science, Soochow University, Suzhou 215123, Jiangsu, China. E-mail: xjfeng@suda.edu.cn; jzhang2017@suda.edu.cn

ORCID: Xinjian Feng (0000-0002-3646-9199), Jun Zhang (0000-0002-9146-9415)

Electrochemical measurement methods

Prior to electrochemical measurements, the electrolyte (0.5 M $KHCO_3$) was sparged with CO_2 at a flow rate of 10 sccm for 30 min to ensure saturation. At this stage, the pH of the solution was 6.8 due to the formation of carbonic acid from dissolved CO_2, resulting in a weakly acidic environment. After completing the hardware check, the electrochemical workstation was initiated. Cyclic voltammetry (CV) was first performed in the potential range from 0.2 to −0.9 V at a scan rate of 50 mV s^{-1} to activate the catalyst. Subsequently, linear sweep voltammetry (LSV) was conducted at 10 mV s^{-1} until stable and overlapping curves were obtained.

In flow cell, the In-3P electrode was directly used as a working electrode, a platinum covered titanium plate and an Ag/AgCl electrode with saturated KCl solution were used as the counter electrode and the reference electrode, respectively. The catholyte and anolyte were each 40 ml of 0.5 M $KHCO_3$ solution circulated using peristaltic pumps at 10 sccm. The H-cell experiments were carried out in a gas-tight two-compartment H-cell separated by a Nafion 117 proton exchange membrane. TheIn-2P was directly used as a working electrode. A carbon rod and a SCE (saturated calomel electrode) with saturated KCl solution were used as the counter electrode and the reference electrode, respectively. For both H-cell and flow cell studies, CO_2 gas flow was controlled by a mass flow controller at 20 sccm, and the applied potentials were Ir-compensated and converted to the RHE scale. The reported partial current densities for CO_2RR were normalized to geometric surface areas. During the long-term stability measured by chronoamperometry of In-3P at −0.9 V and 40°C, the electrolyte refreshed per 4 h.

Production detection

During electrolysis, the generated gas bubbles were directly transferred into the gas sampling loop of a gas chromatograph (Agilent 7890B) for analysis. The concentration of gaseous products was quantified by the integral area ratio of the reduction products to standards. Here we adopt the single standard gas data (Figure S6) to quantify the test gas, repeat our experiments at least for three times, and take the average data to do the

further calculations. Solution phase products were analyzed using an Agilent 400 MHz Nuclear Magnetic Resonance (NMR) spectrometer. Typically, in the quantification of HCOOH, 100 μL of the catholyte was collected after potentiostatic electrolysis, diluted to 10 mL, and filtered through a nylon membrane prior to NMR analysis. Calibration curves were established using standard HCOOH solutions with different concentrations (Figure S7).

Calculation

In CO_2-involved electroreduction reactions, different products are generated depending on the number of electrons transferred. Gaseous products typically include hydrocarbons and CO, while liquid products include formic acid, methanol, ethanol, etc.

For quantitative analysis, the external standard method was employed. Standard gas mixtures containing known concentrations of CO_2, CO, CH_4, C_2H_4, C_2H_6, and H_2 (with N_2 as the carrier gas) were analyzed by gas chromatography (GC) to establish calibration curves. The peak areas of each component were recorded using both the flame ionization detector (FID) and the thermal conductivity detector (TCD).

Gas products generated under different potentiostatic conditions were quantified using a single-point calibration method. The Faradaic efficiency of each gaseous product was calculated according to Equation[1] For example, the Faradaic efficiency of CO (FE-CO) was calculated as follows:

$$FE = \frac{Q_{production}}{Q_{total}} = \frac{n \times F \times t \times [v \times x/(22400 \times 60)]}{i \times t}$$

$$x = x_A \times \frac{S}{S_A}$$

FE: Faradaic Efficiency, representing the fraction of charge consumed for product formation relative to the total charge passed (%).

$Q_{production}$: charge consumed for product formation (C).

Q_{total}: total charge passed (C).

n: number of electrons transferred per mole of product (n = 2 for CO and H_2).

F: Faraday constant, 96485 C/mol.

t: reaction time (s).

v: flow rate of CO_2 in the reaction system (sccm = mL/min).

i: reaction current (A).

x: volume fraction of the product in the analyzed gas mixture.

x_A: volume fraction of the product in the standard gas.

S: integrated chromatographic peak area of the product.

S_A: integrated chromatographic peak area of the standard gas.

22400: molar volume of gas at standard temperature and pressure;

60: conversion factor between minutes and seconds.

Liquid products were generally analyzed by nuclear magnetic resonance (NMR) spectroscopy. For example, for the quantification of HCOOH, 100 μL of catholyte was collected after potentiostatic electrolysis, diluted to 10 mL, and filtered through a nylon membrane prior to liquid-state NMR measurement. Calibration curves were established using HCOOH standard solutions with different concentrations (Figure S7).

The Faradaic efficiency of HCOOH was calculated according to equation followed:

$$FE_{HCOOH} = \frac{Q_{production}}{Q_{total}} = \frac{c \times V \times n \times 96500}{M \times Q}$$

c: the concentration of HCOOH (mg/mL).

V: the volume of the electrolyte (mL).

n: the number of electrons transferred per mole of product (n = 2 for HCOOH).

M: the molar mass of HCOOH (M = 46 g/mol).

Q: the total charge passed during potentiostatic electrolysis (C).

where

c is the concentration of HCOOH (mg mL^{-1});

V is the volume of the electrolyte (mL);

n is the number of electrons transferred per mole of product (n = 2 for HCOOH);

M is the molar mass of HCOOH (M = 46 g mol^{-1});

Q is the total charge passed during potentiostatic electrolysis (C).

The partial current density of products was calculated according to equation followed:

$$J_p = J_{Total} \times FE_p$$

J_p: the partial current density of products (mA/cm^2).

J_{Total}: the total measured current density (mA/cm^2).

The turnover frequency (TOF) of the product represents the number of product molecules generated per active site per unit time. TOF values represent apparent turnover frequencies based on the total moles of In precursor loaded during electrode fabrication, assuming quantitative conversion to metallic In and full accessibility of the catalyst inventory. Taking HCOOH as an example, the calculation method is given by the following equation:

$$TOF = \frac{Q_{Total} \bullet FE_{HCOOH} / nF}{m_{In} / Ar_{In}} \Big/ (t)$$

m_{In}: the mass of In (g).

Ar_{In}: the atomic mass of In.

t: reaction time(t=1h).

Mathematical model

The system is modeled at the continuum scale under the steady-state condition. The computational domain of triphase system consists of four sub-domains, including the liquid diffusion layer (LDL) formed by the analyte, the catalyst layer (CL), the substrate (S), and the gas diffusion layer (GDL) formed by the air. The CL consists of a large number of nanoparticles and is regarded as a porous medium. Transport phenomena outside these regions are considered to have a negligible impact on the system and are not considered. The model incorporates species transport, CO_2 dissolution, and the catalysis reaction. The species transport is described by Fick's law. The CO_2 dissolution from the gas phase to the liquid phase is described by Henry's law. The catalysis

reaction is modeled as first-order kinetics.

In the LDL, the governing equation can be written as,

$$-D_{\mathrm{LDL},i}\nabla^2[i]_\mathrm{l} = 0 \quad \text{(S1)}$$

where $D_{\mathrm{LDL},i}$ is the diffusion coefficient of species i in the LDL, $\mathrm{m^2\ s^{-1}}$; $[i]_\mathrm{l}$ is the concentration of species i in the liquid phase, $\mathrm{mol\ m^{-3}}$. The symbol i denotes three species, i.e., CO_2 and HCOOH.

In the CL, the governing equation can be written as,

$$-D_{\mathrm{CL},i}\nabla^2[i]_\mathrm{l} = R_i \quad \text{(S2)}$$

where $D_{\mathrm{CL},i}$ is the diffusion coefficient of species i in the CL, $\mathrm{m^2\ s^{-1}}$; R_i is the reaction rate of species i, $\mathrm{mol\ m^{-3}\ s^{-1}}$. The symbol i denotes three species, i.e., CO_2 and HCOOH.

The catalysis reaction is modeled as first-order kinetics.

$$R_i = \pm k[\mathrm{CO_2}]_\mathrm{l} \quad \text{(S3)}$$

where k is the reaction rate constant, $\mathrm{s^{-1}}$. The positive value of the R_i represents the production rate of HCOOH, and the negative value represents the consumption rate of CO_2.

In the GDL, since only CO_2 participates in the catalysis reaction, the mass transfer of other species in the gas phase is not considered. The governing equation can be written as,

$$-D_{\mathrm{GDL,CO_2}}\nabla^2[\mathrm{CO_2}]_\mathrm{g} = 0 \quad \text{(S4)}$$

where $D_{\mathrm{GDL,CO_2}}$ is the effective diffusion coefficient of CO_2 in the GDL, $\mathrm{m^2\ s^{-1}}$; $[\mathrm{CO_2}]_\mathrm{g}$ is the concentration of CO_2 in the gas phase, $\mathrm{mol\ m^{-3}}$.

To simulate the mass transfer of CO_2 in the porous media with characteristic lengths that are smaller than the mean free path of CO_2, the Knudsen diffusion must be

considered in the model. The effective diffusion coefficient of oxygen ($D_{\mathrm{GDL,CO_2}}$) is calculated via the Wilke-Bosanquet model[2] ,

$$\frac{1}{D_{\mathrm{GDL,CO_2}}} = \frac{1}{D_{\mathrm{CO_2}}} + \frac{1}{D_{Kn,\mathrm{CO_2}}} \tag{S5}$$

where $D_{\mathrm{CO_2}}$ is the molecular diffusion coefficient of CO_2 in a free environment, $\mathrm{m^2\ s^{-1}}$; $D_{Kn,\mathrm{CO_2}}$ is the Knudsen diffusion coefficient of CO_2 in the gas channel, $\mathrm{m^2\ s^{-1}}$, which can be calculated based on the kinetics theory,

$$D_{Kn,\mathrm{CO_2}} = \frac{d_{\mathrm{pore}}}{3}\sqrt{\frac{8RT}{\pi M_{\mathrm{CO_2}}}} \tag{S6}$$

where d_{pore} is the pore size, m; R is the ideal gas constant, $8.314\ \mathrm{J\ mol^{-1}\ K^{-1}}$; T is system temperature, K; $M_{\mathrm{CO_2}}$ is the molecular weight of CO_2, $0.044\ \mathrm{kg\ mol^{-1}}$.

The computational domain of diphase system consists of four sub-domains, including the liquid diffusion layer (LDL) formed by the analyte, the catalyst layer (CL), the substrate (S). The governing equations for the diphase system are identical to those for the triphase system, except that the governing equations for mass transfer in the gas phase are not required.

All model parameters are listed in Supplementary Table 1 and Supplementary Table 2.

Supplementary Table S1. The geometrical parameters used in numerical simulations

Parameters	Symbols	Units	Values or ranges	References
Pore size	d_{pore}	μm	1	-
Thickness of LDL	δ_{LDL}	μm	50	[3]
Thickness of CL	δ_{CL}	μm	1	-
Thickness of GDL	δ_{GDL}	μm	1	[4]

Supplementary Table S2. The physical parameters used in numerical simulations

Temperature (℃)	Diffusion coefficient of CO_2 in the gas phase (mm^2/s)	Diffusion coefficient of CO_2 in the liquid phase (mm^2/s)	Diffusion coefficient of HCOOH in the liquid phase (mm^2/s)	Solubility of CO_2 in water (g/ 100ml H_2O)
20	16.00025	0.001385552	0.00127	0.1688
30	17.15025	0.001437422	0.00165	0.1257
40	18.30025	0.001489292	0.00201	0.0973
50	19.45025	0.001541162	0.00240	0.0761

As shown in Figure S12, the computational domain of triphase system is divided into four sub-domains: the liquid diffusion layer (Ω_{LDL}), the catalyst layer (Ω_{CL}), the substrate (Ω_S), and the gas diffusion layer (Ω_{GDL}). The boundary indicators are also displayed in Figure S9, where Γ_{LB} is the interface between the LDL and the bulk liquid, Γ_{CL} is the interface between the CL and LDL, Γ_{CG} is the interface between the CL and the GDL, Γ_{GB} is the interface between the GDL and the bulk gas.

At the Γ_{LB}, the concentration of every species is almost equal to the concentration of the corresponding species in the bulk solution. The fixed-value boundary conditions are applied,

$$\begin{cases} [HCOOH]_l = [HCOOH]_{l,b} \\ [CO_2]_l = [CO_2]_{l,b} = H_{CO_2}^{cp} P_{CO_2} \end{cases} \quad (S7)$$

where $[HCOOH]_{l,b}$, and $[CO_2]_{l,b}$ are the concentration of HCOOH and CO_2 in liquid bulk, respectively, they are assumed to remain constant. The HCOOH concentration in liquid bulk is set as 0 because its production is very low and initially there is no HCOOH in the bulk solution. The CO_2 concentration in liquid bulk is equal to the dissolved CO_2 concentration in an aqueous solution. It is calculated by Henry's law, where $H_{O_2}^{cp}$ is Henry's law solubility constant of CO_2, which is defined via equilibrium

concentration in the liquid phase and the equilibrium pressure in the gas phase, mol m^{-3} Pa^{-1}; P_{CO_2} is the partial pressure of CO_2 at 20℃, which can be calculated by Dalton's law of partial pressures.

At Γ_{CL}, the flux of each species through the interface is set to be equal to the outgoing one. The matching condition is applied,

$$-D_{CL,i}\nabla[i]_l = -D_{LDL,i}\nabla[i]_l \quad (S8)$$

where $[i]_l$ is the concentration of species i in the liquid domain.

At Γ_{CG}, the CO_2 must be transported through the triphase interface and dissolved in the liquid before the catalysis reactions take place. It has continuity of the mass flux across the boundary, but the concentration profile of both sides is discontinuous. Henry's law is used to describe the dissolution equilibrium between the gas phase and the liquid phase. The dissolved CO_2 concentration in the liquid phase is calculated by,

$$[CO_2]_l = H^{cp}_{CO_2} p_{CO_2} \quad (S9)$$

where p_{CO_2} is the partial pressure of CO_2, Pa, it is related to the local CO_2 concentration and temperature.

The gas phase is assumed to obey the ideal gas law. Hence, the CO_2 concentration in the gas phase can be calculated based on the partial pressure of CO_2 and the gas temperature,

$$[CO_2]_g = \frac{p_{CO_2}}{RT} \quad (S10)$$

where R is the ideal gas constant, 8.314 J mol^{-1} K^{-1}; T is temperature, K.

Combining equations S9 and S10, it can be found that the CO_2 concentration in the gas phase and the dissolved CO_2 concentration in the liquid phase are subject to an equilibrium relationship,

$$\frac{[CO_2]_l}{[CO_2]_g} = H_{CO_2}^{cp} RT \quad \text{(S11)}$$

The dissolved flux of CO_2 through the GDL is equal to the corresponding absorbed flux entering the CL. The matching condition is applied,

$$-D_{GDL,CO_2} \nabla [CO_2]_g = -D_{CL,CO_2} \nabla [CO_2]_l \quad \text{(S12)}$$

The boundary conditions in equations S11 and S12 enforce the concentration discontinuity condition and maintain flux continuity at the interface between GDL and CL.

At Γ_{GB}, the CO_2 concentration is equal to the CO_2 concentration in the bulk gas. The fixed value boundary condition is applied,

$$[CO_2]_g = [CO_2]_{g,b} \quad \text{(S13)}$$

where $[CO_2]_{g,b}$ is the CO_2 concentration in gas bulk, which is assumed to remain constant.

All other boundaries are applied with zero-flux boundary conditions for each species, which means no mass transfer across these boundaries,

$$-\boldsymbol{n} \cdot (-D_i \nabla [i]) = 0 \quad \text{(S14)}$$

where D_i and $[i]$ are the diffusion coefficient and concentration of each species, respectively.

At the initial state, the HCOOH concentration in the liquid phase ($[HCOOH]_{l,0}$) is equal to the HCOOH concentration in the bulk solution. The CO_2 concentration in the liquid phase ($[CO_2]_{l,0}$) is equal to the initial dissolved CO_2 concentration in the bulk solution. The CO_2 concentration in the gas phase ($[CO_2]_{g,0}$) is equal to the CO_2 concentration in the bulk gas.

$$\begin{cases} [\mathrm{HCOOH}]_{\mathrm{l},0} = [\mathrm{HCOOH}]_{\mathrm{l,b}} \\ [\mathrm{CO_2}]_{\mathrm{l},0} = [\mathrm{CO_2}]_{\mathrm{l,b}} = H^{cp}_{\mathrm{CO_2}} P_{\mathrm{CO_2}} \\ [\mathrm{CO_2}]_{\mathrm{g},0} = [\mathrm{CO_2}]_{\mathrm{g,b}} = \dfrac{P_{\mathrm{CO_2}}}{RT} \end{cases} \quad \text{(S15)}$$

The computational domain of diphase system is divided into four sub-domains: the liquid diffusion layer (Ω_{LDL}), the catalyst layer (Ω_{CL}), and the substrate (Ω_{S}). The boundary conditions of Γ_{LB} and Γ_{CL} are consistent with the corresponding boundary conditions in the triphase system. All other boundaries are applied with zero-flux boundary conditions for each species. The initial conditions are consistent with those of the triphase system.

Figure S1. CA of In-3P electrode.

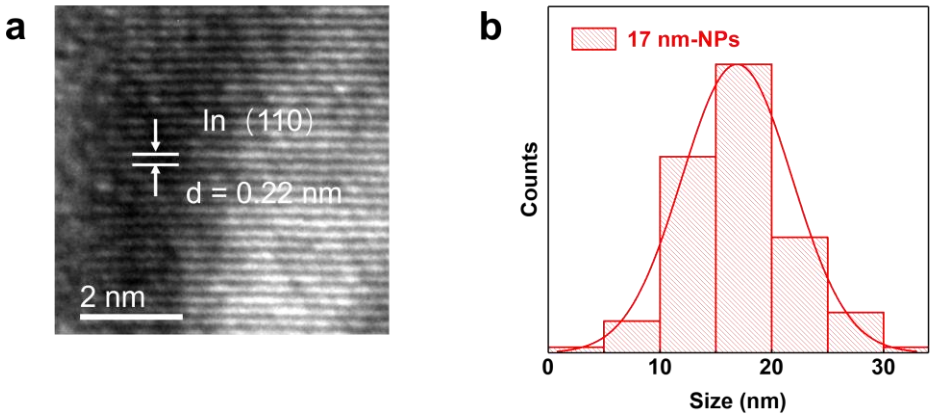

Figure S2. (a) High-resolution transmission electron microscopy (HR-TEM) image of In nanoparticles, with clear lattice fringes corresponding to the (110) plane of metallic indium. (b) Corresponding size distribution histogram of the In nanoparticles.

Figure S3. CA of In-2P electrode.

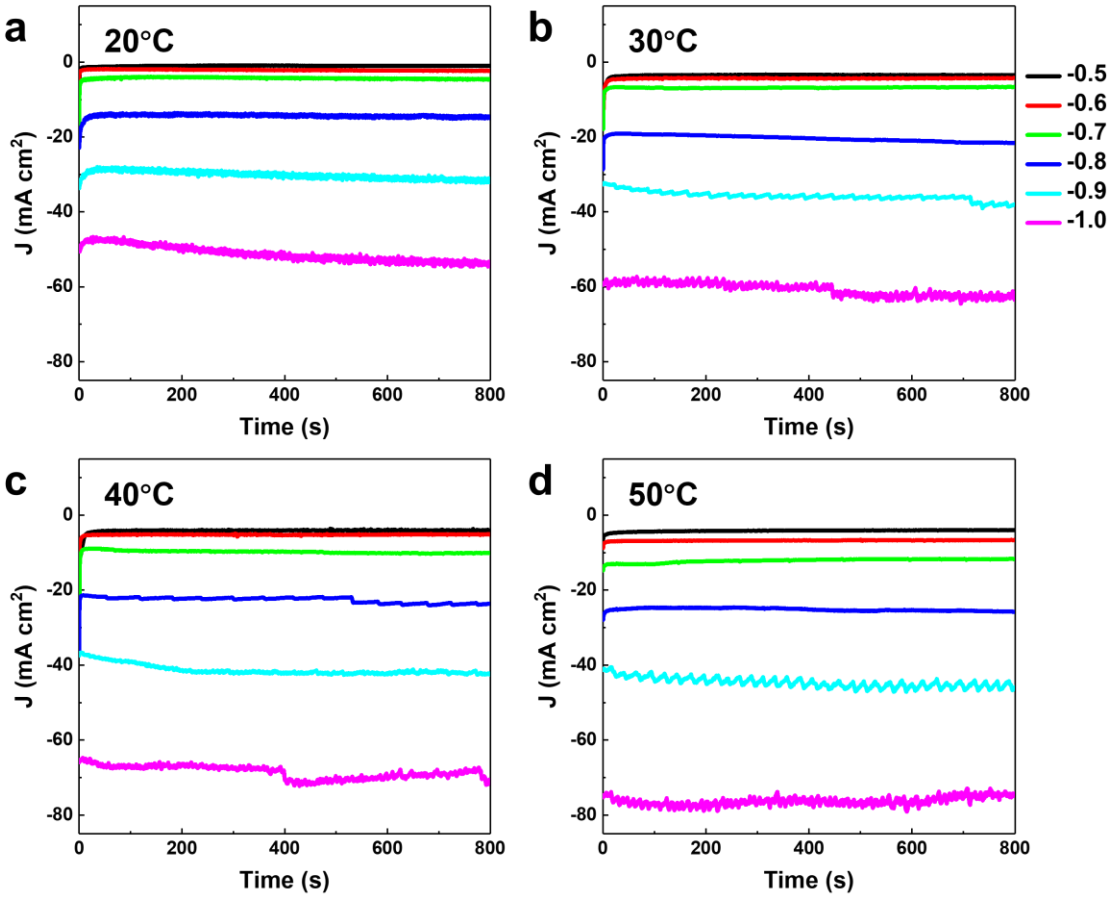

Figure S4. Chronoamperometric curves for eCO_2RR at the In-3P electrode in 0.5 M $KHCO_3$ electrolyte, recorded at applied potentials of −0.5, −0.6, −0.7, −0.8, −0.9 and −1.0 V (vs. RHE) and at (a) 20 °C, (b) 30 °C, (c) 40 °C, and (d) 50 °C.

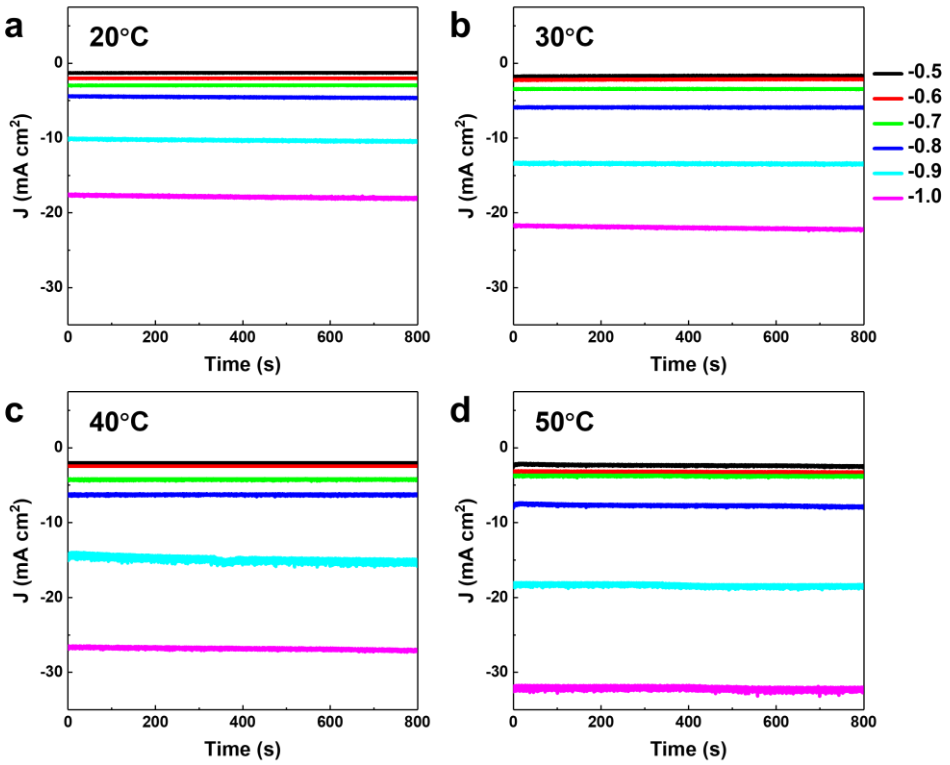

Figure S5. Chronoamperometric curves for eCO$_2$RR at In-2P electrode in 0.5 M KHCO$_3$ electrolyte, recorded at applied potentials of −0.5, −0.6, −0.7, −0.8, −0.9 and −1.0 V (vs. RHE) and at (a) 20 °C, (b) 30 °C, (c) 40 °C, and (d) 50 °C.

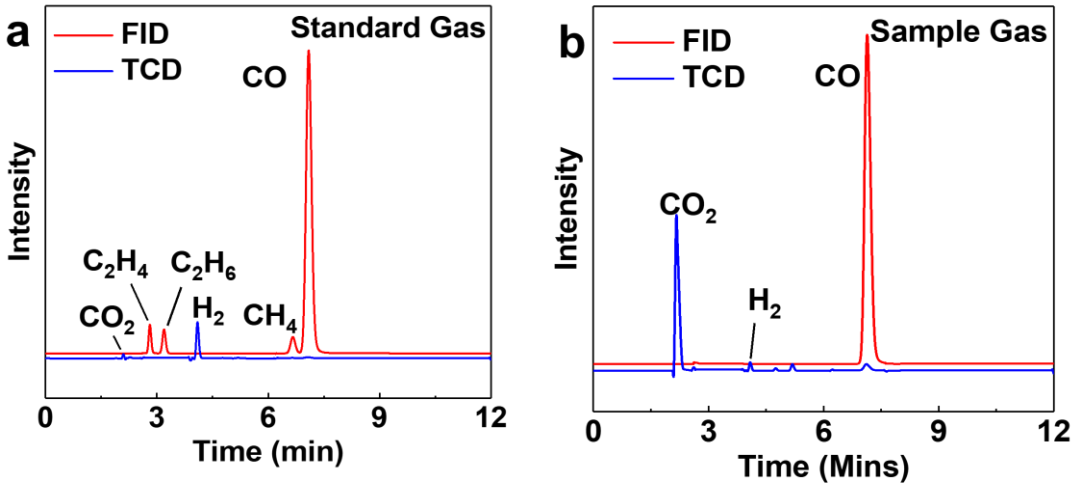

Figure S6. Gas chromatograms of the standard sample (a) and the sample to be analyzed (b).

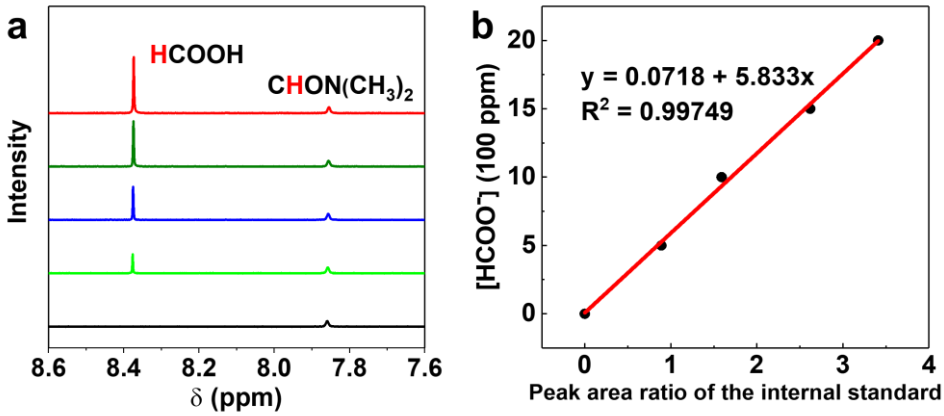

Figure S7. (a) H^1NMR spectra of formic acid standard solutions at different concentrations. (b) Calibration curve of the internal standard.

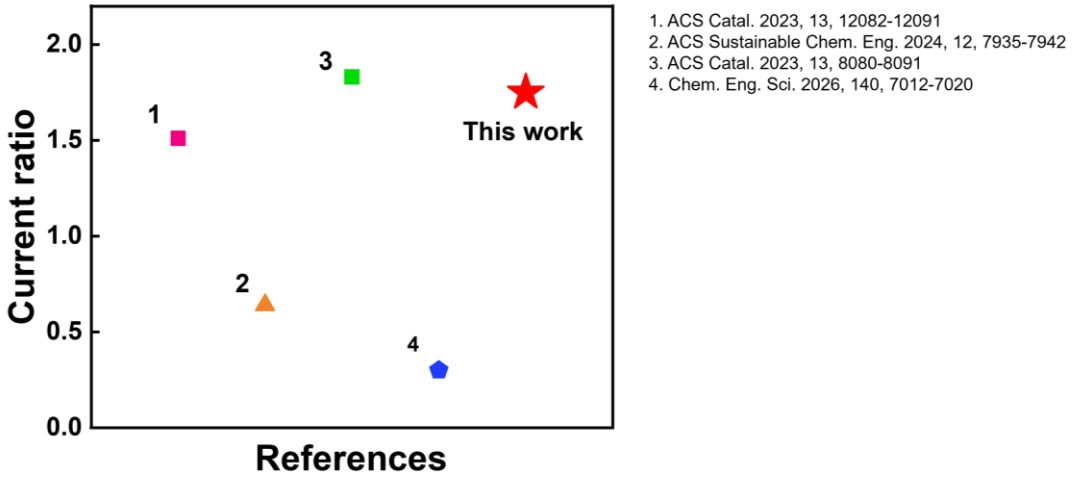

Figure S8. Comparison of current density enhancements achieved through temperature regulation strategies in eCO_2RR systems over recent years with this work[5-8].

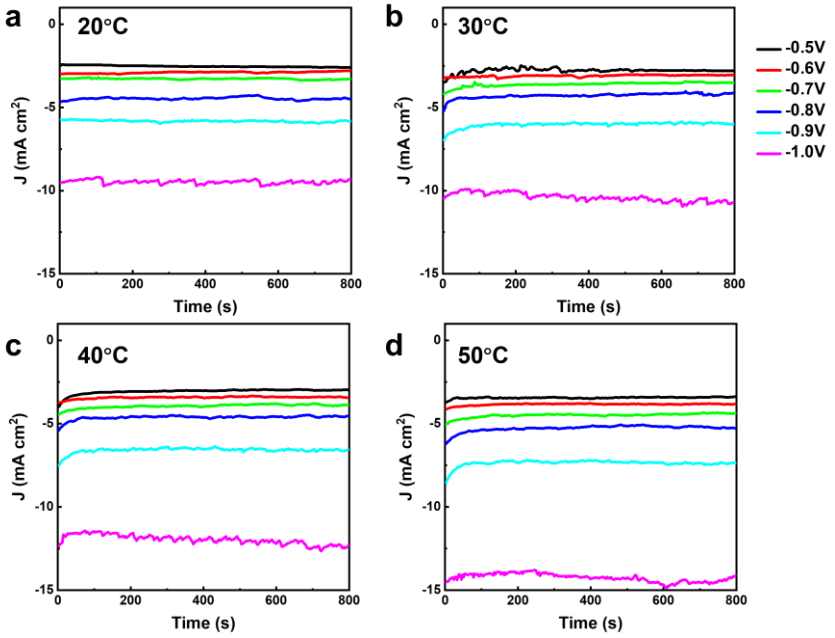

Figure S9. Chronoamperometric curves for eCO$_2$RR at In-3P-N$_2$ electrode in 0.5 M KHCO$_3$ electrolyte, recorded at applied potentials of −0.5, −0.6, −0.7, −0.8, −0.9 and −1.0 V (vs. RHE) and at (a) 20 °C, (b) 30 °C, (c) 40 °C, and (d) 50 °C.

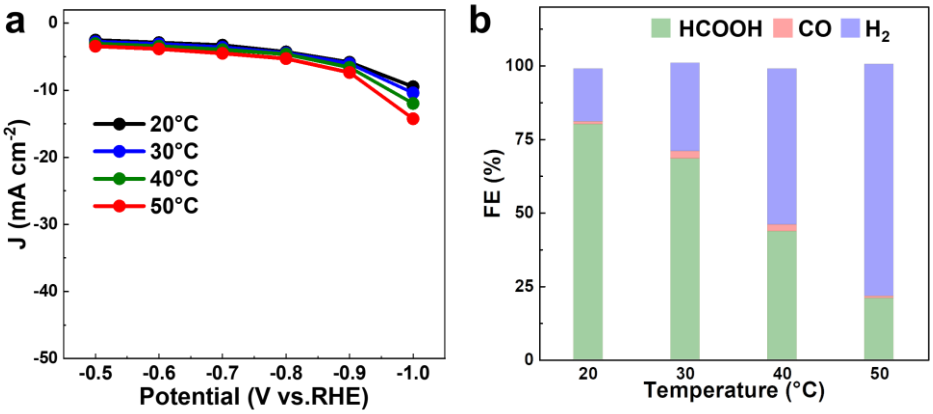

Figure S10. (a) Total current densities for the CO$_2$RR achieved using the triphase In-3P-N$_2$ electrode at various potentials and temperatures. (b) FE of CO$_2$RR products on In-3P-N$_2$ electrode at a potential of -0.9 V vs. RHE and various temperatures.

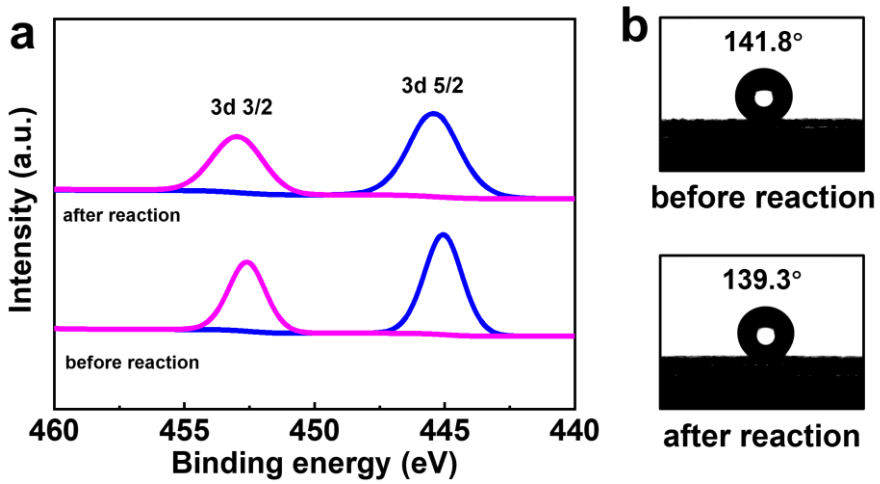

Figure S11. (a) XPS spectra and (b) contact angle images of the catalyst surface before and after a 24 h eCO_2RR stability test

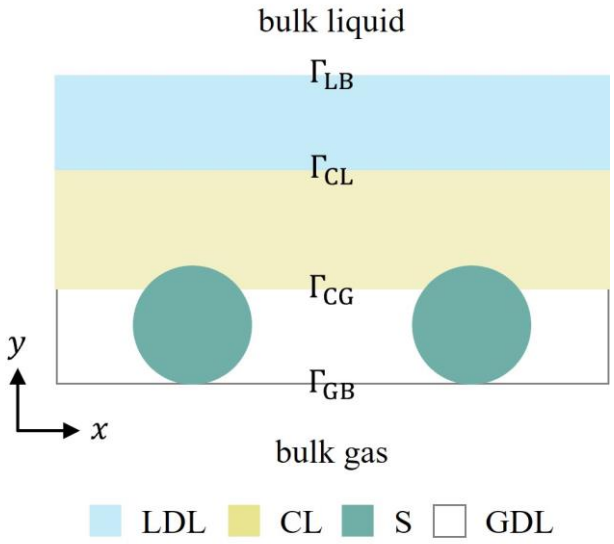

Figure S12. The schematic diagram of the computational domain of triphase system.

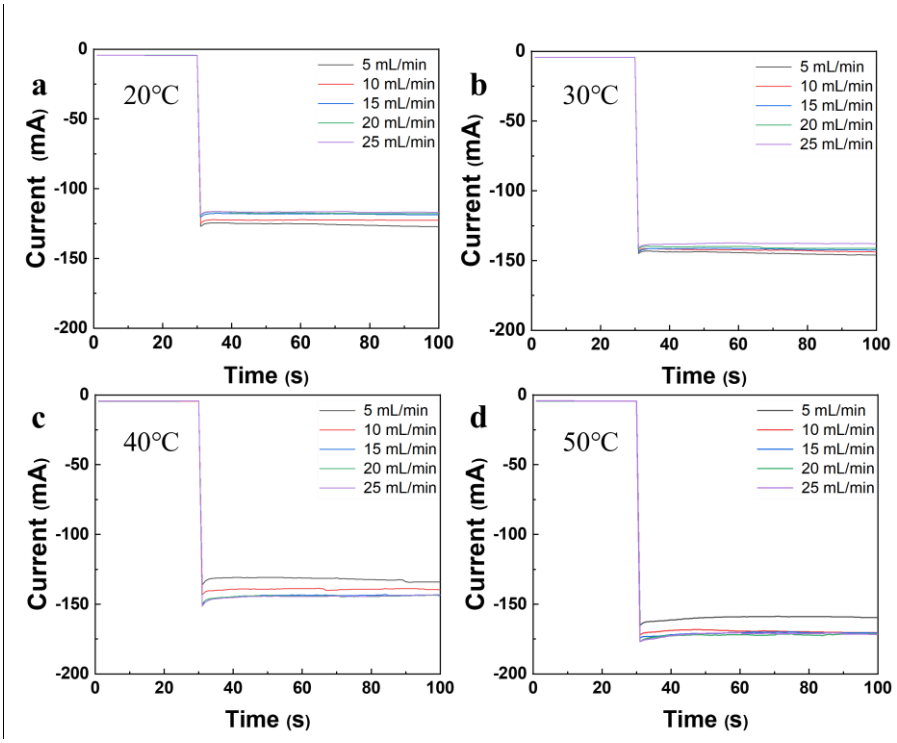

Figure S13. Potential-step chronoamperometric responses of the In-3P electrode from open circuit potential (OCP) to -0.9 V vs. RHE in a flow cell using CO_2-saturated 0.5 M $KHCO_3$ electrolyte at (a) 20 °C, (b) 30 °C, (c) 40 °C, and (d) 50 °C under varying flow rates (5~25 mL min^{-1}).

REFERENCES

1. Clark, E.L.; Bell, A.T. Direct observation of the local reaction environment during the electrochemical reduction of CO_2. *J. Am. Chem. Soc.* **2018**, *140*, 7012-7020, doi:10.1021/jacs.8b04058.

2. Chen, X.-M.; Xiao, J.; Zhu, Y.-P.; Luo, Z.-H. Intraparticle Mass and Heat Transfer Modeling of Methanol to Olefins Process on SAPO-34: A Single Particle Model. *Ind. Eng. Chem. Res.* **2013**, *52*, 3693-3707, doi:10.1021/ie302736b.

3. Baronas, R.; Ivanauskas, F.; Kulys, J. *Mathematical Modeling of Biosensors: An Introduction for Chemists and Mathematicians*, 2 ed.; Springer: Cham, 2021.

4. Weng, L.-C.; Bell, A.T.; Weber, A.Z. Modeling gas-diffusion electrodes for CO_2 reduction. *Phys. Chem. Chem. Phys.* **2018**, *20*, 16973-16984, doi:10.1039/C8CP01319E.

5. Pei, Y.; Gu, W.; Cheng, S.;et al.. Thermo-electrochemically induced dynamic Snδ+/Sn interface for direct bicarbonate reduction to formate. *ACS Catal.* **2023**, *13*, 12082-12091, doi:10.1021/acscatal.3c02630.

6. Rossen, A.; Daems, N.; Choukroun, D.;et.al. Differential pressure across a gas diffusion electrode controls efficiency of liquid-fed electrolyzers for CO_2 electroreduction at elevated temperatures. *ACS Sustainable. Chem. Eng.* **2024**, *12*, 7935-7942, doi:10.1021/acssuschemeng.4c01908.

7. Vos, R.E.; Kolmeijer, K.E.; Jacobs, T.S.;et.al. How temperature affects the selectivity of the electrochemical CO_2 reduction on copper. *ACS Catal.* **2023**, *13*, 8080-8091, doi:10.1021/acscatal.3c00706.

8. Xu, Z.; Shen, C.; Yan, P.;et.al. Temperature-driven selectivity control in bi-catalyzed CO_2 electroreduction via local alkalinity and water structure. *Chem. Eng. Sci.* **2026**, *330*, doi:10.1016/j.ces.2026.123874.